# A DIRECT BLIND SEGMENTATION-TO-UNMIXING METHOD FOR HYPERSPECTRAL IMAGES VIA POLYHEDRAL-CONE PARTITIONING

*Antoine Bottenmuller, Etienne Decencière, and Petr Dokládal*

Mines Paris, PSL University, Centre for Statistics and Images (STIM)
77300 Fontainebleau, France

## ABSTRACT

Two main problems in hyperspectral image analysis are semantic segmentation and unmixing, which are intrinsically linked. The former estimates the material class of each pixel, while the latter estimates the spectral signatures of the materials and their abundances in each pixel in the blind setting. While dominant-material segmentation follows directly from unmixing by selecting the material of largest abundance in each pixel, the reverse mapping remains difficult. Under the linear mixing model, we show that dominant-material classes partition the spectral space into polyhedral cones. We derive from this geometry an unsupervised segmentation-to-unmixing method: a cone partition fitted to an input segmentation provides initial abundances through signed distances, followed by pseudo-inverse recovery of endmembers and final abundances. Combined with pixel clustering, the method outperforms five recent segmentation-guided and learning-based unmixing baselines on Samson and Urban-6.

***Index Terms*—** hyperspectral imaging, blind linear unmixing, semantic segmentation, polyhedral-cone partition

## 1. INTRODUCTION

In remote sensing, hyperspectral imaging systems capture discretized spectral signatures of materials present in an object or a scene, typically representing their absorbance or reflectance spectra, over tens to hundreds of contiguous, narrow bands [1]. For $d$ bands, each pixel of a hyperspectral image (or *dataset*) is an element in the Euclidean space $\mathbb{R}^d$, referred to as the *spectral space* [2], where the $i$-th entry is the spectral response at the $i$-th spectral band.

Limited spatial resolution and scene heterogeneity cause a pixel to mix several materials. Their pure spectra are *endmembers*, their proportions in each pixel are *abundances*, and their relation is described by a mixing model. We consider the standard linear mixing model (LMM) [1, 3].

Two central tasks are *semantic segmentation*, which assigns a material label to each pixel, and *blind unmixing*, which estimates both endmembers and abundances [2]. We focus on *dominant-material* segmentation, where the label of each pixel is the material with maximum abundance in it. Such a map follows directly from unmixing through an abundance $\arg\max$ [4]; the reverse mapping, i.e., from data and labels to unmixing quantities, is more difficult and, to our knowledge, has not been formulated as a general model.

**Contributions.** We propose a direct segmentation-to-unmixing model through a new blind linear unmixing approach that reverses the standard pipeline, bridging semantic segmentation with hyperspectral unmixing. We first prove that, under the LMM, dominant-material classification induces a partition of the spectral space into polyhedral cones. Leveraging this property, and given any segmentation, we fit a polyhedral-cone partition to the labeled pixels and derive an initial abundance estimate via signed distances to the polyhedral regions. This estimate is then used to recover endmembers and final abundances via pseudo-inversion.

Contrarily to existing blind unmixing methods incorporating segmentation information, which use clustering to select *candidate pure pixels* and then apply standard endmember extraction [5, 6], our model derives a direct segmentation-to-unmixing pipeline based on a fundamental polyhedral-based geometric property of dominant-material regions under the LMM that we formalize and prove in this paper. While our method is compatible with supervised segmentation methods, we focus here on unsupervised pixel classification (i.e., clustering) algorithms to perform blind unmixing.

Our reversed-pipeline strategy makes segmentation drive unmixing, giving users explicit control through the choice of segmentation method, while the subsequent steps are lightweight and reproducible. Beyond improving interpretability, the approach opens new paths to hyperspectral unmixing. Experiments on two widely-used real datasets, namely Samson and Urban-6, show consistent improvements over recent deep and non-deep baselines.

## 2. BACKGROUND AND NOTATIONS

### 2.1. The Linear Mixing Model (LMM)

The LMM models the observed data $Y$ as linear combinations of endmembers $M$ weighted by their abundances $A$ [3]. If an

Funded by the Agence Nationale de la Recherche, ANR 22-CE42-0025.

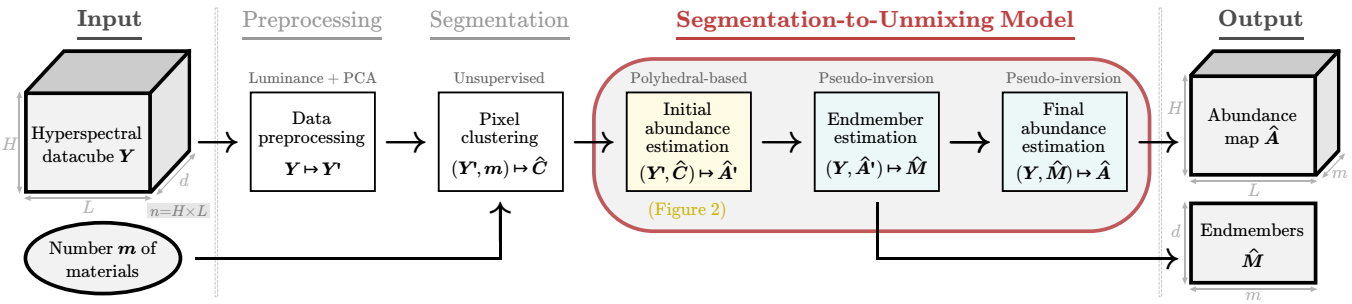



**Fig. 1**. **Method.** Flowchart of blind linear hyperspectral unmixing via our segmentation-to-unmixing approach.

image contains $n$ pixels, each represented by a spectrum of $d$ bands, and is assumed to involve $m$ material endmembers, the LMM is then formulated by the matrix equation

$$Y = MA + E, \tag{1}$$

where $Y \in \mathbb{R}^{d\times n}$ stacks the $n$ pixel spectra; $M \in \mathbb{R}^{d\times m}$ stacks the $m$ endmember spectra; $A \in \mathbb{R}^{m\times n}$ is the abundance matrix (every real $A_{ij}$ is the proportion of the $i$-th endmember in the $j$-th pixel); and $E \in \mathbb{R}^{d\times n}$ is a residual noise matrix with low variance [1]. $A$ satisfies, for all $j = 1, \dots, n$,

$$\begin{cases} A_{ij} \geq 0 \text{ for } i = 1, \dots, m \\ \sum_{i=1}^{m} A_{ij} = 1 \end{cases}. \tag{2}$$

These constraints (2) ensure that the data $Y$, when neglecting noise $E$ in (1), lie within the $(m-1)$-simplex defined by the endmembers $M$ in the spectral space [3].

### 2.2. Standard Blind Linear Unmixing Pipeline.

Given a number $m$ of endmembers, set a priori or determined using a specific method, most blind linear unmixing methods follow a three-step processing chain [1]:

1. **Endmember extraction**: the endmember matrix $\hat{M}$ is estimated from the observed spectral data $Y$ alone.
2. **Abundance recovery**: this *inversion step* estimates the abundance matrix $\hat{A}$ from both $Y$ and $\hat{M}$, typically via matrix inversion, least squares or regression methods.
3. **(Optional) Data labeling**: each pixel can be assigned a dominant-material label by maximum-abundance classification [4]. The class $\hat{C}_j$ of pixel $j$ is given by

$$\hat{C}_j \in \arg\max_{i=1,\dots,m} \hat{A}_{ij}. \tag{3}$$

Pre-processing steps such as luminance correction and dimensionality reduction are usually applied to the dataset $Y$, typically via principal component analysis (PCA) [2].

Our method inverts this traditional unmixing chain.

## 3. SEGMENTATION-TO-UNMIXING MODEL

### 3.1. The Polyhedral-Cone Partition Theorem

We work in the Euclidean spectral space $\mathbb{R}^d$, and begin with the definitions of fundamental geometric objects [7].

**Definition 1** (Polyhedron)**.** A (convex) polyhedron is the intersection of finitely-many closed halfspaces in $\mathbb{R}^d$.

**Definition 2** (Polyhedral Cone)**.** It is a particular polyhedron, whose boundary hyperplanes all pass through the origin $0_d$.

Polyhedral sets, as intersections of halfspaces which are convex sets, are also convex. Based on the data labeling (3) in step (3.) of the standard unmixing chain in Section 2.2, we next formalize the notion of *dominant-material regions*.

**Definition 3** (Dominant-Material Region)**.** Given a class $c$ in $\{1, \dots, m\}$, its dominant-material region $\mathcal{R}_c \subseteq \mathbb{R}^d$ is

$$\mathcal{R}_c := \left\{ x \in \mathbb{R}^d \;\middle|\; c \in \arg\max_{i=1,\dots,m} a_i \right\}, \tag{4}$$

where, for each $x \in \mathbb{R}^d$, the $a_i \in \mathbb{R}$ are the material abundances associated with $x$ over the endmembers $M_{:i} \in \mathbb{R}^d$.

Assuming the endmembers $\{M_{:i}\}_{i=1}^m$ are **linearly independent**, under the LMM, the abundances $a_i$ are exactly the unique linear coefficients $\lambda_i$ of $x$ over the $M_{:i}$, such that

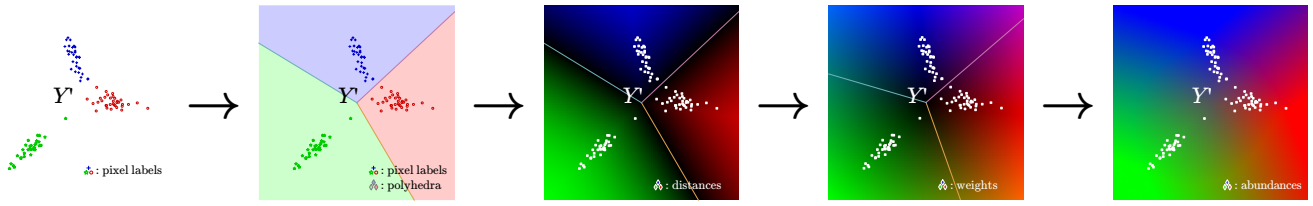
$$x = \sum_{i=1}^{m} \lambda_i M_{:i} + y, \quad y \in (\text{span}\{M_{:i}\}_{i=1}^m)^{\perp}. \tag{5}$$

Each region is thus defined by the $\arg\max$ over the $\lambda_i$, which is preserved under convex combinations. This yields:

**Lemma 1** (Region convexity)**.** *Under linear mixture assumption, dominant-material regions $\mathcal{R}_c$ of $\mathbb{R}^d$ are convex.*

By the Hyperplane Separation Theorem, any two nonempty disjoint convex regions of a Euclidean space can be separated by a hyperplane. This yields our second lemma (see [8]):

**Lemma 2** (Polyhedral Property of Convex Partitions)**.** *Any convex finite ($m$-)partition of a Euclidean space results in $m$ polyhedral regions.*




**Input:** labeled pixels $(Y', \hat{C})$. **Step 1:** polyhedral partitioning. **Step 2:** signed distances. **Step 3:** change of basis. **Step 4:** initial abundance estimate.

**Fig. 2**. Processing chain for initial abundance estimation $\hat{A}'$ via cone partitioning. 2D cross-sections of a 3D spectral space.

Up to a set of Lebesgue measure zero, namely where the $\arg\max$ in (4) is not unique, the dominant-material regions form an $m$-partition of $\mathbb{R}^d$, which, by Lemma 1, is convex. By Lemma 2, these regions are polyhedral. Since the origin $0_d$ has 0 for coefficient on every endmember, it belongs to every region, hence to all separation hyperplanes. We obtain:

**Theorem 1** (Polyhedral-Cone Partition Theorem)**.** *Under the LMM, when $M$ is invertible, the dominant-material regions are $m$ polyhedral cones forming an $m$-partition of $\mathbb{R}^d$.*

This theorem motivates us to start unmixing with the identification of a polyhedral-cone partition of the spectral space that best separates the data labeled by a clustering model.

### 3.2. Method Overview

Our segmentation-to-unmixing method inverts the standard pipeline (Section 2.2). With (i) the original hyperspectral data $Y$ and (ii) their associated material label estimates $\hat{C}$ (resulting from any pixel clustering model on $Y$) as entry points, it outputs both the predicted endmember and abundance matrices $(\hat{M}, \hat{A})$. It comprises three (optionally, four) main stages:

0. **(Optional) Preprocessing ($Y'$).** This stage optionally maps $Y$ to $Y'$. We may (i) normalize spectral luminance to mitigate shadows and illumination effects, and (ii) reduce space dimensionality to $d' < d$ via PCA.

1. **Initial abundance estimation ($\hat{A}'$).** From $Y'$ and $\hat{C}$, we compute an *initial abundance estimate* $\hat{A}'$ via a polyhedral-cone partitioning of the spectral space and a signed distance-based formulation of the abundances. This step uses Theorem 1 as the geometric backbone and represents our main practical contribution. It consists of four steps, developed in the next subsection.

2. **Endmember estimation ($\hat{M}$).** From $Y$ and $\hat{A}'$, the endmember matrix $\hat{M}$ is recovered via matrix pseudo-inversion: $\hat{M} := Y\hat{A}'^{\top}(\hat{A}'\hat{A}'^{\top})^{-1}$.

3. **Final abundance estimation ($\hat{A}$).** We then recover the final abundance matrix $\hat{A}$ from $Y$ and $\hat{M}$ also via pseudo-inversion: $\hat{A} := (\hat{M}^{\top}\hat{M})^{-1}\hat{M}^{\top}Y$.

The pair $(\hat{M}, \hat{A})$ constitutes the final output of our method. Note that in steps (2.,3.), $Y$ is used (not $Y'$), so $\hat{M}_{:i} \in \mathbb{R}^d, \forall i$.

We then may perform blind linear unmixing by combining our segmentation-to-unmixing model with an input clustering method, via the full flowchart illustrated in Figure 1.

### 3.3. Initial Abundance Estimation

The main stage among the three presented in the segmentation-to-unmixing pipeline is the **initial abundance estimation**, which computes an abundance-like matrix $\hat{A}'$, from $Y'$ and $\hat{C}$ alone, using our theoretical results about the polyhedral-cone geometry of the dominant-material regions in the spectral space. It consists of four steps, illustrated in Figure 2:

1. Leveraging Theorem 1, a **polyhedral-cone partition** of the spectral space that best fits the labeled pixels $(Y', \hat{C})$ is estimated, by computing a linear separation hyperplane via an unbiased support vector machine (SVM) for each pair of classes or clusters.

2. For each of the $n$ pixels, its **signed distances** to the $m$ polyhedral-cone regions are computed, as defined in [9] and using the exact nearest-point algorithm in a polyhedral set introduced in the same paper, yielding a distance matrix $D \in \mathbb{R}^{m \times n}$ by stacking the $n$ signed distance vectors defined in the *distance space* $\mathbb{R}^m$, where each coordinate stands for one cone.

3. A **change of basis** is then performed on $D$ in the distance space: $D' := B^{-1}D$, where $B \in \mathbb{R}^{m \times m}$ is the matrix of $m$ reference distance vectors of the regions (as columns of $B$). They can be the vectors of smallest signed distance in each class. This mitigates scale disparities between regions, since larger cones induce greater distances. $D'$ is then a matrix of linear weights.

4. Finally, $D'$ is transformed into an **initial estimate** $\hat{A}'$ that satisfies (2) via the orthogonal projection of the columns of $D'$ onto the probability simplex in $\mathbb{R}^m$. Just before projection, we scale $D'$ ($D' \leftarrow sD'$) by a factor $s > 0$, which controls the *saturation* of the projected data: larger $s$ pushes the points closer to the simplex edges. This is the only hyperparameter of our method.

This main stage is also fully unsupervised, lightweight and—except when extracting a random subset of $Y'$ as input to improve computational results—deterministic.

| Material | Endmember Spectral Angle Distance (SAD) $(\times 10^{-2})$ | | | | | |
|---|---|---|---|---|---|---|
| | SG-VCA | SG-SISAL | MiSiCNet | EDAA | UNMamba | Proposed |
| #1 Soil | 4.31 ± 0.5 | 5.47 ± 0.0 | 1.91 ± 0.2 | 2.87 ± 0.0 | 6.13 ± 0.9 | **1.85 ± 0.2** |
| #2 Tree | 7.53 ± 0.1 | 3.94 ± 0.0 | 5.76 ± 0.0 | 3.45 ± 0.0 | 4.48 ± 0.4 | **3.41 ± 0.1** |
| #3 Water | 11.83 ± 5.3 | 15.26 ± 0.0 | 9.45 ± 0.1 | **2.28 ± 0.0** | 3.38 ± 0.1 | 2.93 ± 0.2 |
| Avg. | 7.89 ± 1.9 | 8.22 ± 0.0 | 5.71 ± 0.1 | 2.87 ± 0.0 | 4.66 ± 0.2 | **2.73 ± 0.1** |
| Material | Abundance Root Mean Square Error (RMSE) $(\times 10^{-2})$ | | | | | |
| | SG-VCA | SG-SISAL | MiSiCNet | EDAA | UNMamba | Proposed |
| #1 Soil | 10.48 ± 2.0 | 8.42 ± 0.0 | 6.76 ± 0.3 | 5.73 ± 0.0 | 12.55 ± 0.6 | **4.18 ± 0.3** |
| #2 Tree | 9.71 ± 3.9 | 6.45 ± 0.0 | 5.42 ± 0.3 | 3.76 ± 0.0 | 10.55 ± 0.7 | **3.05 ± 0.2** |
| #3 Water | 5.94 ± 2.5 | 4.80 ± 0.0 | 3.59 ± 0.1 | **2.59 ± 0.0** | 2.61 ± 0.1 | 3.33 ± 0.2 |
| Avg. | 8.71 ± 2.8 | 6.56 ± 0.0 | 5.26 ± 0.2 | 4.03 ± 0.0 | 8.57 ± 0.4 | **3.52 ± 0.2** |

**Table 1**. The SADs and RMSEs (mean±std) on Samson. The best values are in bold; the second-best are underlined (/row).

| Material | Endmember Spectral Angle Distance (SAD) $(\times 10^{-2})$ | | | | | |
|---|---|---|---|---|---|---|
| | SG-VCA | SG-SISAL | MiSiCNet | EDAA | UNMamba | Proposed |
| #1 Asph. | 19.30 ± 2.9 | 5.26 ± 0.0 | 12.98 ± 0.0 | 4.34 ± 0.0 | 18.44 ± 0.2 | **3.50 ± 0.2** |
| #2 Grass | 37.48 ± 4.3 | 14.97 ± 0.0 | 18.36 ± 0.0 | 19.74 ± 0.0 | 16.27 ± 0.3 | **5.08 ± 0.1** |
| #3 Tree | 34.39 ± 5.3 | 22.61 ± 0.0 | 16.62 ± 0.0 | 19.73 ± 0.0 | 8.50 ± 0.0 | **7.48 ± 0.2** |
| #4 Roof | 77.45 ± 8.6 | 20.99 ± 0.0 | 23.53 ± 0.0 | 17.79 ± 0.0 | 6.92 ± 0.1 | **6.59 ± 0.6** |
| #5 Metal | 30.65 ± 0.0 | 19.20 ± 0.0 | 15.61 ± 0.0 | 44.70 ± 0.0 | 22.66 ± 0.2 | **11.58 ± 0.8** |
| #6 Dirt | 34.93 ± 9.6 | 56.87 ± 0.0 | 34.06 ± 0.0 | 18.75 ± 0.0 | **10.25 ± 0.4** | 11.17 ± 0.2 |
| Avg. | 39.03 ± 1.5 | 23.32 ± 0.0 | 20.19 ± 0.0 | 20.84 ± 0.0 | 13.84 ± 0.1 | **7.57 ± 0.2** |
| Material | Abundance Root Mean Square Error (RMSE) $(\times 10^{-2})$ | | | | | |
| | SG-VCA | SG-SISAL | MiSiCNet | EDAA | UNMamba | Proposed |
| #1 Asph. | 20.83 ± 8.8 | 21.15 ± 0.0 | 18.86 ± 0.0 | 15.33 ± 0.0 | 19.37 ± 0.2 | **10.40 ± 0.3** |
| #2 Grass | 31.10 ± 3.5 | 25.15 ± 0.0 | 20.37 ± 0.0 | 43.24 ± 0.0 | **14.76 ± 0.1** | 18.63 ± 0.2 |
| #3 Tree | 15.79 ± 1.1 | 24.20 ± 0.0 | 12.26 ± 0.0 | 21.63 ± 0.0 | 12.96 ± 0.5 | **11.15 ± 0.1** |
| #4 Roof | 15.84 ± 1.9 | 14.22 ± 0.0 | 7.12 ± 0.0 | **4.82 ± 0.0** | 8.23 ± 0.3 | 8.58 ± 0.3 |
| #5 Metal | 13.95 ± 2.2 | 13.31 ± 0.0 | 9.11 ± 0.0 | 35.64 ± 0.0 | 9.60 ± 0.3 | **8.34 ± 0.4** |
| #6 Dirt | 38.42 ± 9.9 | 30.96 ± 0.0 | 25.00 ± 0.0 | **13.09 ± 0.0** | 19.30 ± 0.5 | 15.38 ± 0.3 |
| Avg. | 22.65 ± 2.1 | 21.50 ± 0.0 | 15.45 ± 0.0 | 22.29 ± 0.0 | 14.04 ± 0.2 | **12.08 ± 0.2** |

**Table 2**. The SADs and RMSEs (mean±std) on Urban-6. The best values are in bold; the second-best are underlined (/row).

## 4. EXPERIMENTS

We evaluate our segmentation-to-unmixing model, combined with an input clustering method to perform unsupervised segmentation, in the blind setting on Samson (containing 3 materials) and Urban-6 (containing 6 materials) datasets [10].

### 4.1. Benchmark Methods

We compare the results with five state-of-the-art unmixing algorithms, across two families:

- **Segmentation-guided geometrical methods.** We use a segmentation-guided (SG-) version of two geometrical methods using the SLIC-derived preprocessing endmember candidate selection method developed in [6]: a pure-pixel algorithm, VCA [11], and a minimum-volume one, SISAL [12], among the most effective [1].
- **Deep learning-based methods.** We use two autoencoders, (i) MiSiCNet [13], which incorporates geometrical information, and (ii) a recent cascaded spatial-spectral Mamba-based model (UNMamba) [14]; and Entropic Descent Archetypal Analysis (EDAA) [10] which uses an entropic descent algorithm to solve the Archetypal Analysis problem.

MiSiCNet, EDAA and UNMamba have been shown to outperform prior deep and non-deep methods [13, 10, 14], making them competitive baselines.

### 4.2. Evaluation Metrics

To evaluate the unmixing quality, we consider two standard metrics: (i) the spectral angle distance (SAD) for endmembers, and (ii) the root mean square error (RMSE) for abundances [13]. Let $i \in \{1, \dots, m\}$ denote the index of the material among the observed ones to evaluate.

The SAD between the predicted endmember $\hat{M}_{:i} \in \mathbb{R}^d$ and the associated ground-truth $M_{:i} \in \mathbb{R}^d$ is defined as

$$\mathrm{SAD}(\hat{M}_{:i}, M_{:i}) = \arccos\left(\frac{\langle \hat{M}_{:i}, M_{:i} \rangle}{\|\hat{M}_{:i}\| \|M_{:i}\|}\right). \tag{6}$$

It measures the angle (radians) between two vectors in $\mathbb{R}^d$.

The RMSE between the predicted abundance $\hat{A}_{i:} \in \mathbb{R}^n$ and its associated ground-truth $A_{i:} \in \mathbb{R}^n$ is defined as

$$\mathrm{RMSE}(\hat{A}_{i:}, A_{i:}) = \sqrt{\frac{1}{n}\sum_{j=1}^{n}(\hat{A}_{ij} - A_{ij})^2}. \tag{7}$$

It quantifies per-pixel error. For both metrics, lower is better.

### 4.3. Experimental setup

Our method is implemented in Python.[1]

**Hyperparameter $s$.** Based on an ablation study made on Samson and Urban-6 datasets, we propose the following formula for the simplex *saturation* hyperparameter $s$:

$$s = \left(3 \cdot \mathrm{std}(D')^2 \cdot m\right)^{-4},$$

where $\mathrm{std}(D')$ is the standard deviation of the elements of $D'$, and $m$ the number of materials in the observed scene.

**Semantic segmentation.** To prove the flexibility of our model with different clustering methods, we test it on two of them, each for one dataset. For Samson, we use a Gaussian mixture model (GMM) fitted on a random $25\%$ data sampling. For Urban-6, since the dataset is more challenging to segment, we use the EGFSC-AXBW hyperspectral clustering algorithm [15]. For comparison fairness, we use the same input segmentation maps for the segmentation-guided (SG-) versions of VCA and SISAL as the ones used for our method.

**Sampling for SVM.** To improve performance, we fit SVMs on a random $15\%$ to $25\%$ pixel subset of $Y'$. This induces variation in unmixing results from one run to another.

**Baselines.** We use the publicly-available codes provided in [10, 14] and in the HySUPP Python package [1], using the settings recommended by the authors of the original papers.

### 4.4. Results

Tables 1 and 2 report the resulting SADs and RMSEs for each material (rows), as well as the average value (Avg.) over all

[1] Code: https://github.com/antoine-bottenmuller/polyhedral-unmixing.git

materials in the last row, for every tested method (columns). The means and standard deviations (mean±std) over 10 runs per experiment are given in each cell. For every row, the best results are shown in bold and the second best are underlined.

Our method achieves the best average SAD and RMSE on both datasets and the best result for most individual materials. It remains near-best otherwise, and runs in 0.7 s on Samson and 1.6 s on Urban-6. Thus, with an appropriate input clustering method, it outperforms both deep and non-deep baselines, especially on the more challenging Urban-6 scene.

## 5. CONCLUSION

We introduced an unsupervised segmentation-to-unmixing model that reverses the standard blind linear unmixing pipeline. Its core theorem shows that, under the LMM, dominant-material regions partition the spectral space into polyhedral cones. Fitting these cones to segmented data and exploiting signed distances yields endmember and abundance estimates with a single saturation hyperparameter.

Combined with clustering, the method improves over two segmentation-guided geometrical and three strong learning-based baselines on Samson and Urban-6 while remaining lightweight. Future work will quantify sensitivity to segmentation quality and incorporate the polyhedral-cone prior into direct endmember estimation or deep learning architectures.

## 6. REFERENCES


[1] Behnood Rasti, Alexandre Zouaoui, Julien Mairal, and Jocelyn Chanussot, "Image processing and machine learning for hyperspectral unmixing: An overview and the hysupp python package," *IEEE Transactions on Geoscience and Remote Sensing*, 2024.

[2] José M Bioucas-Dias, Antonio Plaza, Gustavo Camps-Valls, Paul Scheunders, Nasser Nasrabadi, and Jocelyn Chanussot, "Hyperspectral remote sensing data analysis and future challenges," *IEEE Geoscience and remote sensing magazine*, vol. 1, no. 2, pp. 6–36, 2013.

[3] José M Bioucas-Dias, Antonio Plaza, Nicolas Dobigeon, Mario Parente, Qian Du, Paul Gader, and Jocelyn Chanussot, "Hyperspectral unmixing overview: Geometrical, statistical, and sparse regression-based approaches," *IEEE journal of selected topics in applied earth observations and remote sensing*, vol. 5, no. 2, pp. 354–379, 2012.

[4] Edurne Ibarrola-Ulzurrun, Lucas Drumetz, Javier Marcello, Consuelo Gonzalo-Martín, and Jocelyn Chanussot, "Hyperspectral classification through unmixing abundance maps addressing spectral variability," *IEEE Transactions on Geoscience and Remote Sensing*, vol. 57, no. 7, pp. 4775–4788, 2019.

[5] Gabriel Martin and Antonio Plaza, "Spatial-spectral preprocessing prior to endmember identification and unmixing of remotely sensed hyperspectral data," *IEEE journal of selected topics in applied earth observations and remote sensing*, vol. 5, no. 2, pp. 380–395, 2012.

[6] Xiang Xu, Jun Li, Changshan Wu, and Antonio Plaza, "Regional clustering-based spatial preprocessing for hyperspectral unmixing," *Remote Sensing of Environment*, vol. 204, pp. 333–346, 2018.

[7] George Phillip Barker, "Theory of cones," *Linear Algebra and its Applications*, vol. 39, pp. 263–291, 1981.

[8] Emerson León and Günter M Ziegler, "Spaces of convex n-partitions," in *New Trends in Intuitive Geometry*, pp. 279–306. Springer, 2018.

[9] Antoine Bottenmuller, Florent Magaud, Arnaud Demortière, Etienne Decencière, and Petr Dokladal, "Euclidean distance to convex polyhedra and application to class representation in spectral images," in *14th International Conference on Pattern Recognition Applications and Methods*. SCITEPRESS-Science and Technology Publications, 2025, pp. 192–203.

[10] Alexandre Zouaoui, Gedeon Muhawenayo, Behnood Rasti, Jocelyn Chanussot, and Julien Mairal, "Entropic descent archetypal analysis for blind hyperspectral unmixing," *IEEE Transactions on Image Processing*, vol. 32, pp. 4649–4663, 2023.

[11] José MP Nascimento and José MB Dias, "Vertex component analysis: A fast algorithm to unmix hyperspectral data," *IEEE transactions on Geoscience and Remote Sensing*, vol. 43, no. 4, pp. 898–910, 2005.

[12] José M Bioucas-Dias, "A variable splitting augmented lagrangian approach to linear spectral unmixing," in *First workshop on hyperspectral image and signal processing: Evol. in remote sensing*. IEEE, 2009, pp. 1–4.

[13] Behnood Rasti, Bikram Koirala, Paul Scheunders, and Jocelyn Chanussot, "Misicnet: Minimum simplex convolutional network for deep hyperspectral unmixing," *IEEE Transactions on Geoscience and Remote Sensing*, vol. 60, pp. 1–15, 2022.

[14] Dong Chen, Junping Zhang, and Jiaxin Li, "Unmamba: Cascaded spatial-spectral mamba for blind hyperspectral unmixing," *IEEE Geoscience and Remote Sensing Letters*, 2025.

[15] Yongshan Zhang, Xinxin Wang, Xinwei Jiang, Lefei Zhang, and Bo Du, "Elastic graph fusion subspace clustering for large hyperspectral image," *IEEE Transactions on Circuits and Systems for Video Technology*, 2025.